

Spatial inversion symmetry breaking of vortex current in a biased-ladder superfluid

Weijie Huang¹ and Yao Yao^{1,2,*}

¹*Department of Physics, South China University of Technology, Guangzhou 510640, China*

²*State Key Laboratory of Luminescent Materials and Devices, South China University of Technology, Guangzhou 510640, China*



(Received 31 July 2023; revised 19 December 2023; accepted 21 December 2023; published 11 January 2024)

We investigate the quench dynamics of interacting bosons on a two-leg ladder in the presence of a uniform Abelian gauge field. The model hosts a variety of emergent quantum phases, and we focus on the superfluid biased-ladder phase breaking the Z_2 symmetry of two legs. We observe an asymmetric spreading of vortex current and particle density, i.e., the vortices propagate ballistically on the right and dissolve during the propagation on the left, indicating spontaneous breaking of the spatial inversion symmetry. By decreasing the repulsion strength, it is found that the ballistic propagating vortices are more robust than the dissolving ones on the other side.

DOI: [10.1103/PhysRevResearch.6.013037](https://doi.org/10.1103/PhysRevResearch.6.013037)

I. INTRODUCTION

Lattice gauge theory (LGT), an equivalent form of gauge field, has manifested advantages in comprehending many effects in condensed matter physics [1]. Enormous progresses of quantum computations in the last decade have then stimulated intense research activities to explore the possibility of encompassing LGTs [2–7]. Currently, proposals have been made in a couple of platforms, including cold atoms in optical lattices, trapped ions, Rydberg atoms, and superconducting qubits [8–21], and proof-of-principle experimental realizations of lattice gauge fields have been conducted [22–28].

A specific type of gauge field, known as background (or static) gauge field [29–32], has drawn significant attention [33–45]. This field, together with proper interactions, generate an extensive collection of many-body phases with remarkable properties, such as superconductivity and Mott insulators. With the experimental developments in synthetic dimension and artificial gauge fields, one-dimensional quantum simulators provide convenient realizations of higher-dimensional quantum models [32,46,47], such as the Harper-Hofstadter model [33,36,37,40,42,47]. The edge states of the two-dimensional Hofstadter model are found to be repetitions of ladder eigenstates with an exponential decay, indicating that the band structure of a two-leg ladder can be traced back to the edge states of the Hofstadter model [48]. These studies have paved ways for investigating other scenarios including both bosonic and fermionic ladders under Abelian fields. Moreover, properties beyond the phase diagram of the multileg flux ladders remains active lines of research, e.g., the

possible existence of Laughlin-like states [45,49–51] and the calculation [52] and measurement [53–55] of Hall effect. Research interests were further extended to the nonequilibrium dynamics by imposing a quantum quench [8,21,28,54,56–60]. The dynamics of particles was simulated, e.g., two repulsively interacting bosons on a real-space flux ladder [28]. The sensitivity of model parameters and initial states has been noticed in the short-time dynamics, which is essential in experimental simulations [21,28,54,56,57].

As shown in a landmark study based on bosonization in 2001 [61], the Meissner and vortex phases, which are reminiscent of a type-II superconductor, are found in the two-leg flux-ladder model. A variety of emergent quantum phases are hosted by the bosonic flux ladders in presence of on-site interaction [50,61–77], including Meissner phase, vortex-liquid phase, vortex lattice phase, the charge-density wave (CDW) phase, and the biased-ladder phase (BLP). The configurations of local currents $\langle j_{\ell,r}^{\parallel} \rangle$ and $\langle j_r^{\perp} \rangle$ serve as one of the most important quantities to distinguish the phases [67]. The Meissner phase possesses a finite uniform chiral leg current encircling the ladder while the rung current vanishes. Currents in CDW and BLP are very similar with that in the Meissner phase but would break some discrete symmetries [67]. In the vortex phases, the rung currents on the inner rungs develop, forming vortices in the system depressing the chiral current. Except CDW, other phases can be further divided into two phases, superfluid and Mott insulator, which can be characterized by calculating the central charge, as well as the entanglement entropy [56,67]. More interestingly, the main characteristics of BLP turns out to be the finite leg-population imbalance, stabilized by the interchain interactions [56]. In the thermodynamic limit the ground state would thus be twofold degenerate, and the subsequent Z_2 symmetry in terms of inversion of two legs and the signs of relevant flux is spontaneously broken [67]. Considering these remarkable features lead to exotic dynamical effects, therefore, we focus on the superfluid BLP phase in the present work.

*yaoyao2016@scut.edu.cn

Published by the American Physical Society under the terms of the [Creative Commons Attribution 4.0 International license](https://creativecommons.org/licenses/by/4.0/). Further distribution of this work must maintain attribution to the author(s) and the published article's title, journal citation, and DOI.

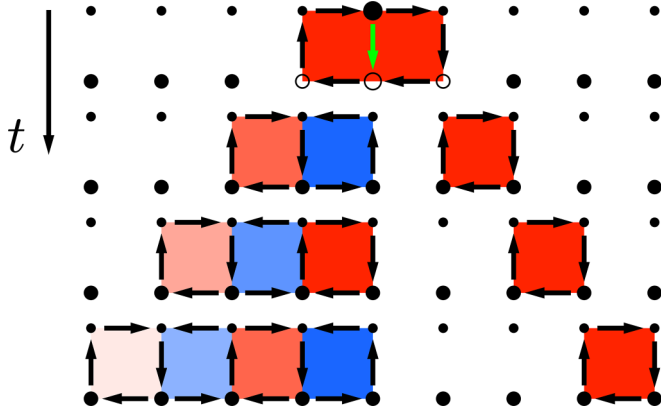


FIG. 1. Sketch of the rung current excitation creating asymmetric spreading process. Typical states on the ladder at four instant points are drawn from top to bottom. At $t = 0$, the rung current excitation operator (green arrow) is applied to the BLP ground state. The local population is denoted by the size of dots and the exhausted population is denoted by empty circles. The deviations of the currents from the background chiral currents are represented by black arrows. The red and blue squares label the clockwise and counterclockwise vortices, respectively, and the color depth indicates the magnitude of the vortex current.

II. METHODOLOGY

A. Model

As sketched in Fig. 1, the Hamiltonian of a paradigmatic two-leg flux-ladder model is given by

$$\begin{aligned}
 H = & -J \sum_{r=1}^{L-1} \sum_{\ell=1}^2 (a_{\ell,r}^\dagger a_{\ell,r+1} + \text{H.c.}) \\
 & -J_\perp \sum_{r=1}^L (e^{-ir\phi} a_{1,r}^\dagger a_{2,r} + \text{H.c.}) \\
 & + \frac{U}{2} \sum_{r=1}^L \sum_{\ell=1}^2 n_{\ell,r} (n_{\ell,r} - 1) + V \sum_{r=1}^L n_{1,r} n_{2,r}, \quad (1)
 \end{aligned}$$

which is residing on a ladder with L rungs. Herein, the local operator $a_{\ell,r}^\dagger$ ($a_{\ell,r}$) creates (annihilates) a boson on the lower ($\ell = 1$) or the upper ($\ell = 2$) leg of the r th rung and $n_{\ell,r} = a_{\ell,r}^\dagger a_{\ell,r}$; J and J_\perp are nearest-neighbor hopping constants along legs and rungs, respectively; ϕ is the flux per ladder plaquette; the bosons also have on-site repulsion U and interchain repulsion V . We define the filling as $f = N/(2L)$, where N is the total number of bosons. Throughout this work, we set $\phi = 0.85\pi$, $J = 1$, $J_\perp = 3$, $U = 2$, $f = 0.8$, the lattice constant $a = 1$, and $\hbar = 1$. By this setting, the system has been determined to reside in the superfluid BLP phase [67], which is essential to produce the symmetry breaking as discussed below, and we always choose the ground state with lower leg population larger than upper.

It is worth noting that the model possesses a gauge freedom that one can choose different Peierls phase factors as long as the total flux of a single ladder plaquette remains invariant. The chosen gauge described by Hamiltonian

Eq. (1) is a so-called rung gauge in which the hopping matrix elements on the legs are real and on the rungs are complex.

By the Heisenberg equation of motion $\frac{dn_{\ell,r}}{dt} = i[H, n_{\ell,r}]$, we define a local current operator on legs as

$$j_{\ell,r}^\parallel = iJ(a_{\ell,r}^\dagger a_{\ell,r+1} - a_{\ell,r+1}^\dagger a_{\ell,r}), \quad (2)$$

and the current operator on the rung as

$$j_r^\perp = iJ_\perp (e^{-ir\phi} a_{1,r}^\dagger a_{2,r} - e^{ir\phi} a_{2,r}^\dagger a_{1,r}). \quad (3)$$

It is also convenient to define a background chiral current

$$j^{\text{ch}} = \frac{1}{L-1} \sum_{r=1}^{L-1} (j_{1,r}^\parallel - j_{2,r}^\parallel) \quad (4)$$

to characterize the average current circulating the ladder along the legs.

B. Methods

The ground-state results are calculated by using the density-matrix renormalization group (DMRG) method [78–81]. We simulate the flux ladder up to $L = 200$ rungs and the bond dimension is typically up to 1000. The existence of repulsive interactions allows us to employ a cutoff for the maximum number of local boson states. We keep at most four local boson states and have also checked that with six and eight states, which produce consistent results (see Appendix C). The subsequent time evolution is then simulated via time-evolving block decimation (TEBD) method [82–84]. For the simulations in the main text, we set fixed discarded weight $\text{cutoff} = 10^{-6}$ and maximum bond dimension $\chi = 1000$ to reach long times. Once the maximum bond dimension is reached, we continue the simulation with fixed bond dimension which will lead to increased numerical errors. To quantify the uncertainties, we present the convergence tests with respect to the number of local boson states and maximum bond dimension χ in Appendix C. Even though deviations of local observables already start to emerge at times $t < 15$, the asymmetry is observed in the spreading throughout the convergence tests. More data and detailed discussion can be found in Appendix C.

C. Quantum quench

Let us first describe the main scenario we are investigating as displayed in Fig. 1. The BLP ground state hosts a finite uniform anticlockwise chiral leg current encircling the ladder and vanishing rung current. A single rung in the middle is then excited to generate vortex current at time $t = 0$ by applying a rung current operator without phase factor to the superfluid BLP ground state, i.e., $i(a_{1,L/2}^\dagger a_{2,L/2} - a_{2,L/2}^\dagger a_{1,L/2})|\psi_0\rangle$. In other relevant works [56,65] where the internal atomic states are identified with the legs of the ladder [spin up correspond to the upper leg ($\ell = 2$) and spin down correspond to the lower leg ($\ell = 1$)], $a_{1,L/2}^\dagger a_{2,L/2}$ becomes $a_{\downarrow,L/2}^\dagger a_{\uparrow,L/2}$ which flips the local spin up to spin down. Therefore, the rung current operator used in our quench protocol $i(a_{\downarrow,L/2}^\dagger a_{\uparrow,L/2} - a_{\uparrow,L/2}^\dagger a_{\downarrow,L/2})$ is a spin-flip operator like σ^y which could be implemented by the lasers in the experiments. Nevertheless, the experimental

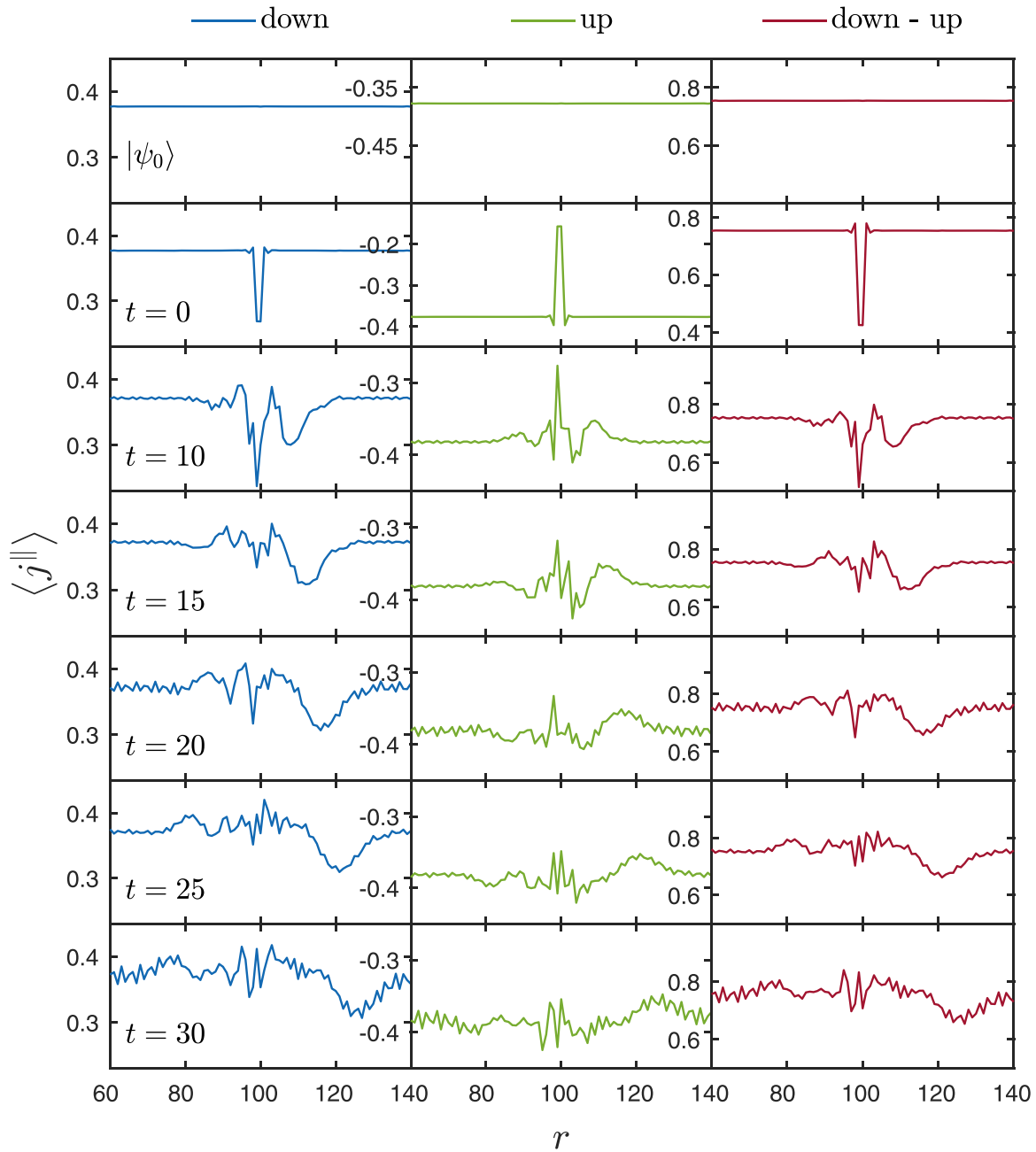


FIG. 2. Snapshots of the time evolution of local leg current configurations $\langle j_{\ell,r}^{\parallel} \rangle$ with $V = 3$ after the initial rung current excitation. “Charge” current $\langle j_r^c \rangle$ is shown in the rightmost column, whose deviation from mean values quantifies the leg currents of the vortices.

preparation of BLP ground states is difficult, making the exploration of dynamics under our quench protocol challenging.

III. RESULTS

The excitation creates accumulation of populations on the upper leg ($\ell = 2$) which we call “particle” (bigger dots) and three sites with exhausting populations on the lower leg ($\ell = 1$) as we call “holes” (circles). This leads to current change on top of background chiral currents which generates two adjacent clockwise vortices (red squares) with current (black arrow) on the edge. On the right side, the “particle” moves along the same direction with the upper leg current of clockwise vortex making them constructive and

move outwards ballistically like a solitary wave or a particle. On the left side, however, the concentration of “hole” and “particle” oscillate between two neighboring sites on the same rung, which is similar to the recombination process of majority and minority carriers in semiconductors. The corresponding rung current oscillates between up and down legs in the same fashion, giving rise to a vortex on the initial position alternating between clockwise and counterclockwise. In addition, vortices with opposite directions are destructive, so they move forward diffusively following with quick decay. This resembles how plane water waves spread. In short, vortices propagate ballistically on the right and dissolve during the propagation on the left in just one ladder.

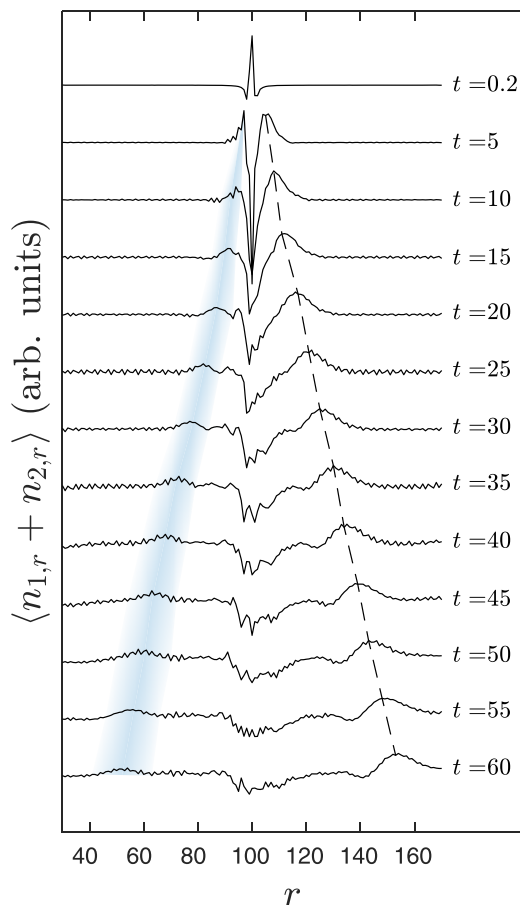


FIG. 3. Snapshots of time evolution of the charge concentration configurations $\langle n_r^c \rangle = \langle n_{1,r} + n_{2,r} \rangle$ with $V = 3$. The shaded region shows the approximate location of wavepacket of vortices on the left side and the dashed line indicates the propagation of the wavepacket of vortices on the right side.

Snapshots of current configurations in the time evolution after rung current excitation are shown in Fig. 2. The initial current excitation generates deviations of the local currents both on the upper leg $\langle j_{2,r}^{\parallel} \rangle$ and lower leg $\langle j_{1,r}^{\parallel} \rangle$ at $t = 0$. The deviations of the current then form the vortices spreading out towards the two directions. The deviations in the two legs are shown to be always almost identical in magnitude but the signs are different. Hence, in order to manifest the symmetry breaking of spatial inversion, we define a “charge” current $\langle j_r^c \rangle = \langle j_{1,r}^{\parallel} - j_{2,r}^{\parallel} \rangle$ to fingerprint the vortices. It is observed that the central “charge” current behaves like a source, emitting vortices outward and moving. Positive and negative vortices alternate and oscillate on the left side, while there is visibly a big solitary vortex propagating ballistically on the right side: The asymmetry appears.

We relevantly calculated the quench dynamics of the same local rung current operator applied to the ground states of other phases. The results (for details, see Appendix A, Fig. 5) show that the asymmetry is absent in other phases, making it an exclusive signature of the biased-ladder phase (BLP).

We similarly calculate the population configurations on each leg $\langle n_{\ell,r} \rangle$ (see Appendix C, Fig. 8) which symmetrically

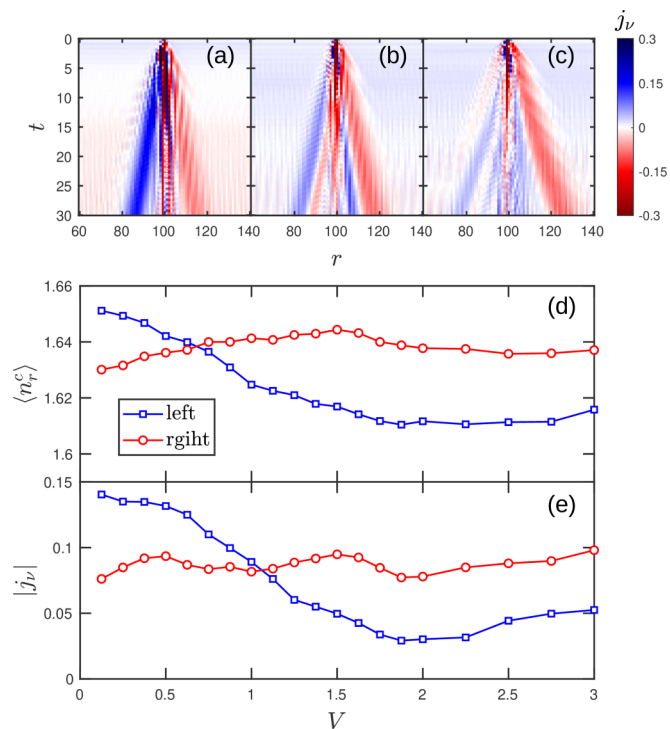


FIG. 4. The net “charge” current j_v and “charge” concentration $\langle n_r^c \rangle = \langle n_{1,r} + n_{2,r} \rangle$ in spreading of vortices with various V . The wavepackets of the two counter-propagating vortices are shown in different colors. (a)–(c) time evolution of j_v with $V = 0.125$, $V = 1.125$, and $V = 3$. The maximum points of $\langle n_r^c \rangle$ and j_v at $t = 30$ are shown in (d) and (e).

spread out from the central site. To see the asymmetric influence of chiral current, we define the relevant “charge” concentration as $\langle n_r^c \rangle = \langle n_{1,r} + n_{2,r} \rangle$. As shown in Fig. 3, after the wavepacket splits into two counter-propagating parts, the main part of the wavepacket on the left is blocked by the chiral current and the minor spreading part decays quickly. On the other hand, the decay of the right wavepacket is much slower. More importantly, regardless of the slight broadening, a distinguishable solitary wavepacket shape is always reserved. This visible asymmetry significantly exhibiting the spreading of “charge” is inversion symmetry broken in space. In essence, the vortices on both sides are accompanied by local “charge” concentrations whose deviation from mean values are proportional to that of the local “charge” currents. Therefore, both the “charge” concentration $\langle n_r^c \rangle$ and the “charge” current $\langle j_r^c \rangle$ can fingerprint the vortices. We can also simultaneously define the “spin” concentration as $\langle n_r^s \rangle = \langle n_{1,r} - n_{2,r} \rangle$, which reflects the local population imbalance between the two legs. The spreading of the “spin” concentration is symmetric, which differs from that of the “charge” concentration (see Appendix C for more details). Namely, the influence that the vortices exerted on the local leg-population imbalance is not proportional to the local charge concentrations, indicating the influence is almost the same for the ballistic propagating vortices and the dissolved vortices.

To figure out the origin of this asymmetric spreading, the parameter of interchain repulsion V is changed. Figure 4 shows the net current $j_v = \langle j_r^c - j_r^{\text{ch}} \rangle$ and the maximum point

of “charge” concentration (n_r^c) of the two counter-propagating vortices. From Figs. 4(a)–4(c), one can clearly see that following the increase of V , the net current on the left is fading while it is fairly stable on the right. That is, with small V , the net current of the left wave is larger than the right one, and with large V , the left current fades and the spreading then prefers the right side. The asymmetric fading facilitates the imbalance of the two sides which mainly leads to the asymmetric spreading. In addition, the speeds on the two sides are roughly equal and linear with time.

As described above, the excitation creates the “particle” and “holes” which spread from the central rung creating a counterclockwise vortex (blue in Fig. 1) moving left and a clockwise vortex (red in Fig. 1) moving right. It is essential that the counterclockwise vortex enlarges the chiral current j^{ch} while the clockwise vortex suppresses it. For cases with small V , the spreading of “particle” and “hole” will weaken the imbalance of leg population so that the system is almost close to the Meissner phase. Since the chiral current grows monotonically from BLP to Meissner phase [56,67], the counterclockwise vortex (blue in Fig. 1) will be mutually enhanced with the chiral current. Following the increase of V , the chiral current is suppressed and the imbalance of leg population is then stabilized. As a consequence, the counterclockwise vortex is decreased, and when V exceeds a certain value, the “particles” and “holes” on the left side are almost blocked and difficult to spread out. In this situation, the concentrations of “hole” and “particle,” together with the corresponding rung current, start to oscillate on the same rung. On the other hand, considering that the clockwise vortex always decreases the chiral current, V does not matter on it. Therefore, the clockwise vortex moving right overtakes and becomes more robust than the counterclockwise vortex moving left. It is counterintuitive, as the clockwise vortex suppressing the chiral current j^{ch} can propagate ballistically while the counterclockwise vortex enlarging the chiral current will be weakened and dissolve in the propagation.

IV. CONCLUSION

In summary, we have studied the time evolution of vortex current and concentration in a superfluid BLP phase. An asymmetric spreading of the vortex current is found determined by the direction of background chiral current. Further simulations reveal that, as the interchain repulsion increases, the vortices on the left side are suppressed, while those on the right side remain robust. This disparity directly leads to the asymmetry of the spreading. Interestingly, the ballistically propagating vortices are reminiscent of the ballistic moving operator front in the emergent dissipative hydrodynamics [85–89] of operator spreading in Ref. [86], where the results are obtained in a random quantum circuit model that is constrained to have a conservation law. It would be intriguing to explore a more effective description of vortex spreading, potentially leading to connections between our findings and the theories of operator spreading. Besides, with the rapid development in the experimental techniques, the ballistic propagating current might prove useful in future experimental implementations of flux ladders exploiting dynamical problems.

ACKNOWLEDGMENT

The authors gratefully acknowledge support from the Key Research and Development Project of Guangdong Province (Grant No. 2020B0303300001), and National Natural Science Foundation of China (Grants No. 11974118 and No. 12374107).

APPENDIX A: QUENCH DYNAMICS OF OTHER PHASES

We relevantly calculated the quench dynamics of the same local rung current operator applied to the ground states of other phases, i.e., $i(a_{1,L/2}^\dagger a_{2,L/2} - a_{2,L/2}^\dagger a_{1,L/2})|\psi_0\rangle$. In terms of the results shown in Fig. 5, the relevant spreading patterns for initial states in Meissner, vortex liquid, and vortex lattice phases are all symmetric, even if they have some minor differences with each other. The asymmetric spreading is the specific signature of BLP phase based on the current calculation results we received. Comparing the details of the relevant spreading process for different initial phases might be an interesting study in the future but requires more comprehensive calculations and analyses, which is beyond the scope of present work.

As the CDW phase exists in the regimes of large U , we did not try to discuss the spreading process after the local quench. The asymmetric spreading is the specific signature of BLP phase based on the current calculation results we have determined. Comparing the details of the relevant spreading process for different initial phases might be an interesting study in the future but requires more comprehensive calculations and analyses which is beyond the scope of present work.

APPENDIX B: ENTANGLEMENT ENTROPY

In this section, we present the time evolution of the von Neumann entanglement entropy, defined as $S_{\text{vN}} = -\text{Tr}[\rho \ln(\rho)]$ with ρ being the reduced density matrix by cutting both two legs at the same points to divide the ladder into two halves. The results are shown in Fig. 6, which are calculated at the fixed discarded weight ($\text{cutoff} = 10^{-6}$) with $L = 80$. One can find that, as well fitted by a logarithmic function, the entropy grows logarithmically with time, which is the typical increase brought by a local quench [90–94].

APPENDIX C: DETAILS ON NUMERICAL DATA

In this section we present additional data and give more details on the numerical quality of the time-evolution simulations.

The time evolution of ladder system to long times are hard to calculate considering the system sizes are rather large, as $L = 200$. We tried to use a smaller system size ($L = 80$) to reduce the computational costs. In terms of our tests, even for $L = 80$ keeping discarded weight $\text{cutoff} = 10^{-6}$ needs maximum bond dimension χ up to 5000 at $t = 8.5$ and 10000 at $t = 10$ which are not affordable to continue. In this regard, the entanglement entropy is only calculated to $t = 8.0$ at the fixed discarded weight ($\text{cutoff} = 10^{-6}$) with $L = 80$.

The observation of the spreading process will be affected by the boundary effects in a small system as the wavefront gets too close to the boundaries at early times. To vividly

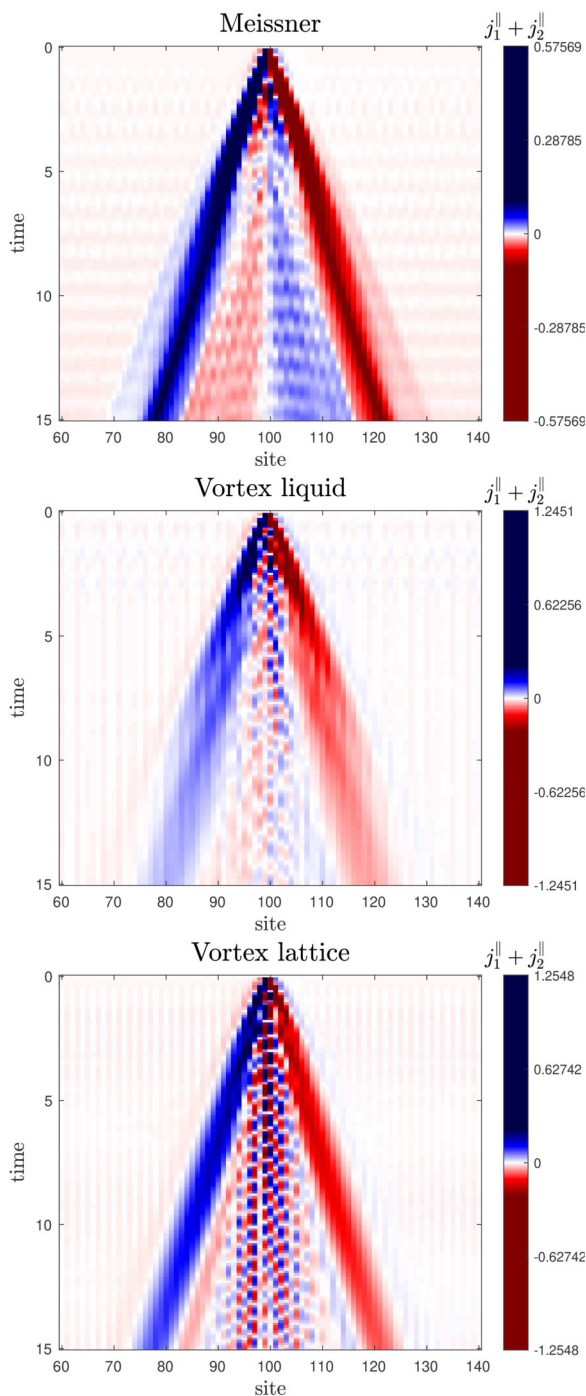


FIG. 5. The time evolution of $\langle j_{1,r}^{\parallel} + j_{2,r}^{\parallel} \rangle$ for three different initial states. From top to bottom: the Meissner phase ($\phi = 0.6\pi$, $J_{\perp} = 3.0$, $V = 2$), the vortex liquid phase ($\phi = 0.8\pi$, $J_{\perp} = 1.6$, $V = 0$), and vortex lattice phase ($\phi = 0.95\pi$, $J_{\perp} = 1.6$, $V = 0$). $U = 2$, $f = 0.8$ consistent with the calculation in the main text, $L = 200$.

depict the asymmetric spreading process, where vortices propagate ballistically on one side and dissolve while propagating to the other side, extending the simulation time and allowing vortices to travel longer distances becomes necessary. Consequently, we utilized a larger system ($L = 200$) and extended our simulations to longer times ($t = 30$ and even $t = 60$) for the calculations of the local observables in the main

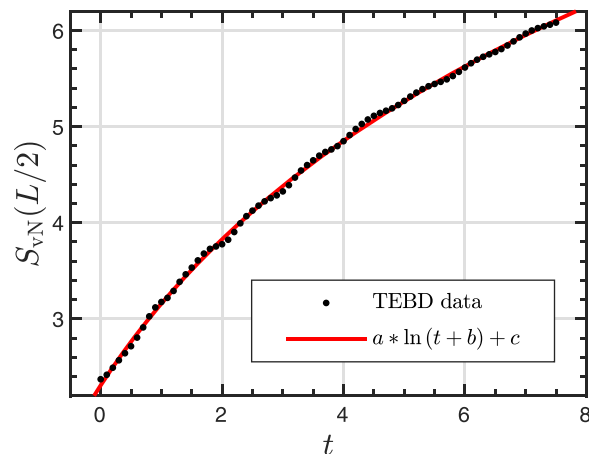


FIG. 6. Time evolution of the von Neumann entanglement entropy for the central bipartition $S_{vN}(L/2)$. The blue line represents the obtained curve with the coefficients $a = 3.1829$, $b = 3.2637$, and $c = -1.4585$ after fitting the data with a logarithmic function of the form $a \ln(t + b) + c$. The system size is $L = 80$ and $V = 3$.

text. We can only set a fixed discarded weight ($cutoff = 10^{-6}$) and restrict maximum bond dimension ($\chi = 1000$) simultaneously to keep the time cost affordable. That is to say, initially, we run the program with a fixed discarded weight of $cutoff = 10^{-6}$. However, if the needed bond dimension exceeds $\chi = 1000$, we will not longer increase the bond dimension. Instead, we continue the simulations with the fixed bond dimension ($\chi = 1000$). It should be noted that this will reduce numerical accuracy and may lead to potentially uncontrolled errors.

To quantify uncertainties, we conduct convergence tests with respect to χ and the maximum numbers of local boson states. The results are shown in Figs. 7–10. In Figs. 7 and 8, we calculated the particle densities and currents for $L = 200$ with different numbers of local boson states. The time evolution of the “spin” concentration $\langle n_r^s \rangle = \langle n_{1,r} - n_{2,r} \rangle$ is shown in Fig. 8, which reflects the local population imbalance between the two legs. The spreading of the “spin” concentration is symmetric, and differs from that of the “charge” concentration. The results in Figs. 7 and 8 indicate that using four local boson states reduces accuracy, causing small deviations in currents, whereas the results obtained with six to ten local boson states appear to converge. In Fig. 9, $\chi = 1500, 2000$ are calculated and compared with the data taken from Figs. 2 and 3 in the main text. Larger χ up to 4000 are also calculated in a smaller system ($L = 80$) for comparison which is shown in Fig. 10. In the tests with respect to χ in Figs. 9 and 10, the deviations in currents become increasingly pronounced as time progresses. The comparisons indicate that employing larger local dimensions and different numbers of local boson states already leads to deviations in the currents at $t < 15$, while the local particle densities exhibit better convergence in the comparison. Nevertheless, the asymmetric spreading can always be observed among the tests with different control parameters.

Next, we tried to simulate at fixed discarded weight without restricting the maximum bond dimension. A smaller system $L = 80$ was simulated with different numbers of local boson states (4, 6, and 8). Considering the computational costs, our simulation was conducted up to $t = 10$ where keeping

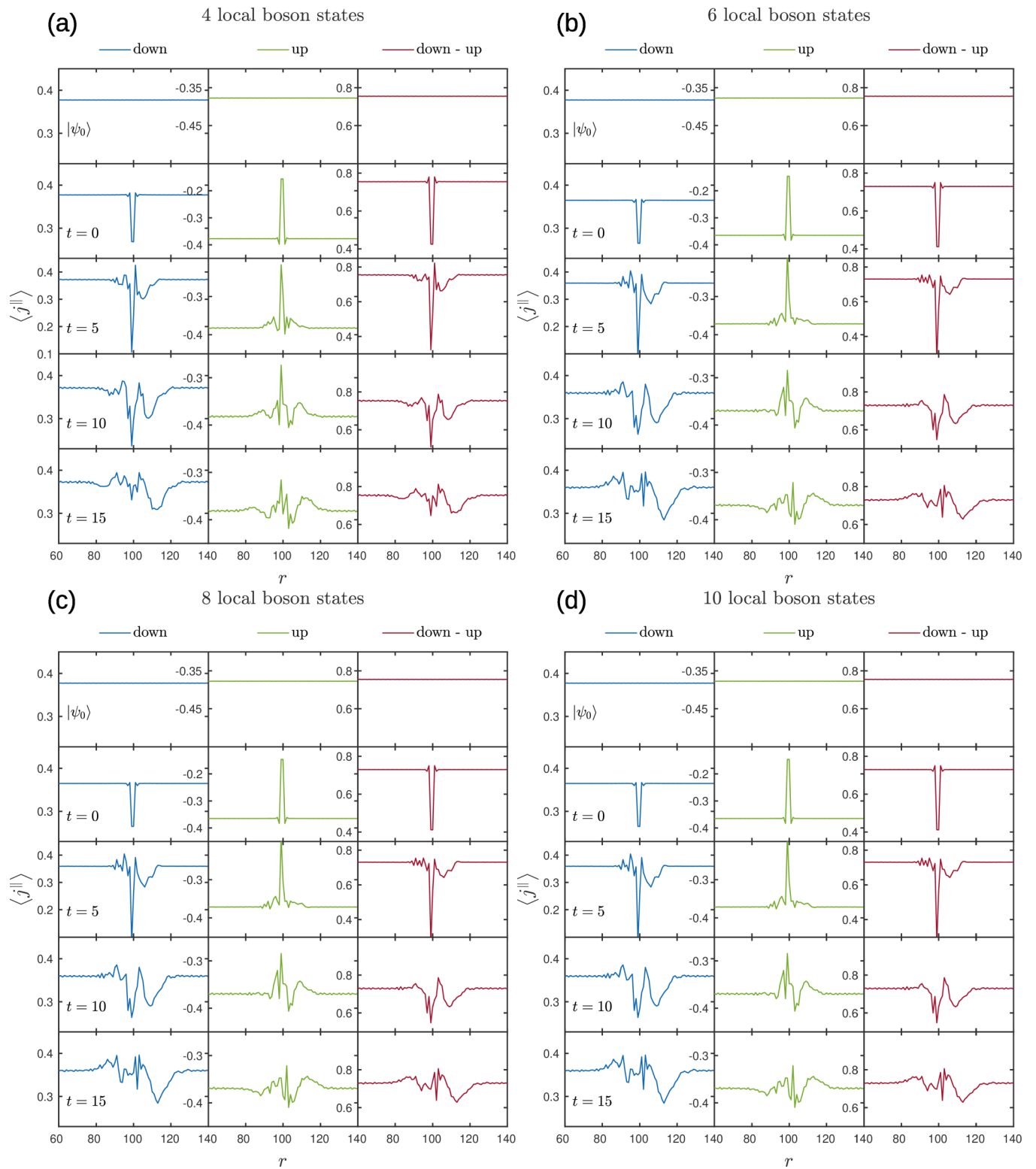


FIG. 7. Snapshots of the time evolution of local leg current configurations $\langle j_{\ell,r}^{\parallel} \rangle$ with varying numbers of local boson states: (a) 4 states, (b) 6 states, (c) 8 states, and (d) 10 states. Here, $L = 200, V = 3, \chi = 1000$, and other parameters consistent with the manuscript.

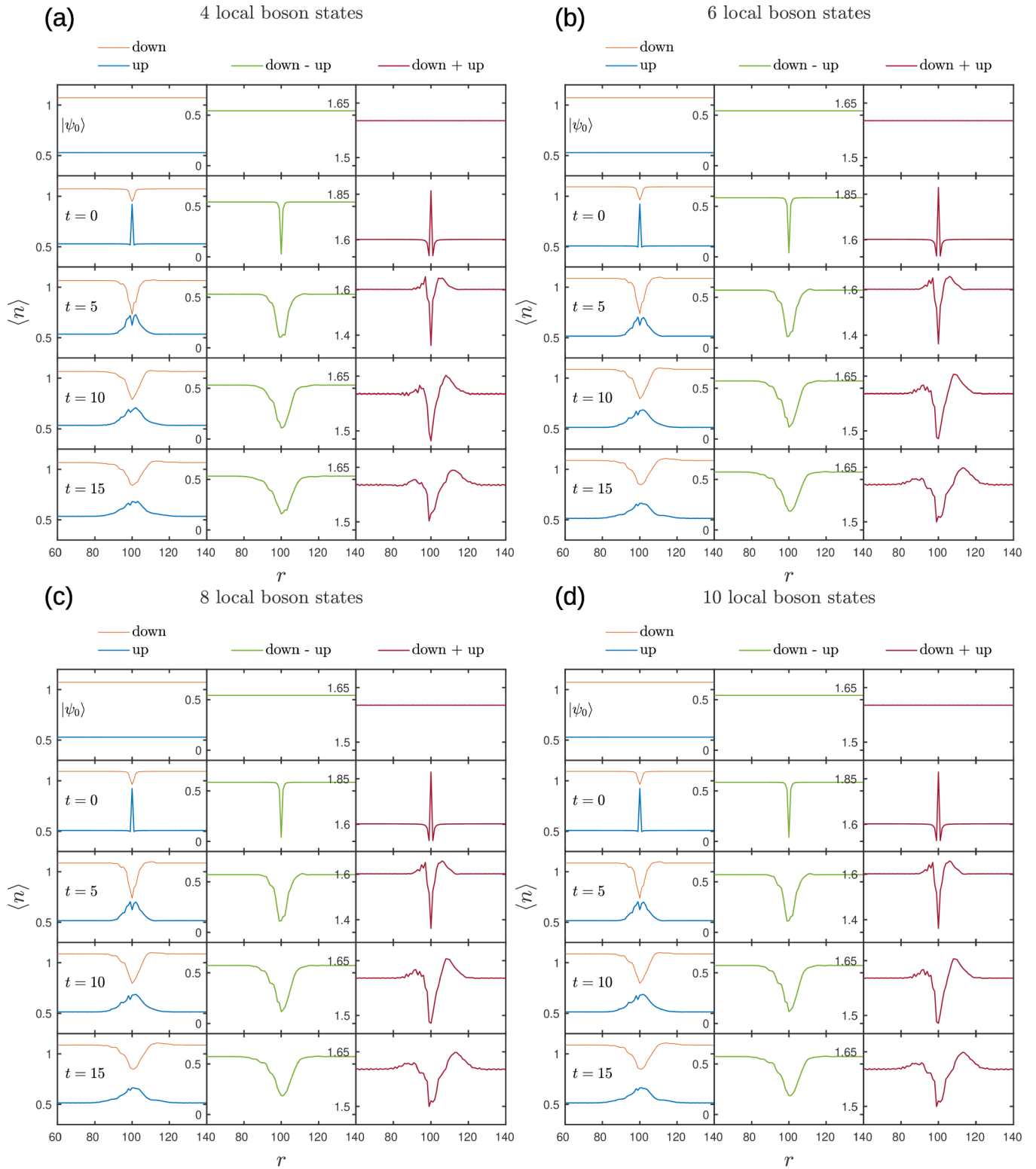


FIG. 8. Snapshots of the time evolution of local particle density $\langle n_{\ell,r}^{\parallel} \rangle$, the spin concentration configurations $\langle n_r^s \rangle = \langle n_{1,r} - n_{2,r} \rangle$, and the charge concentration configurations $\langle n_r^c \rangle = \langle n_{1,r} + n_{2,r} \rangle$ with varying numbers of local boson states: (a) 4 states, (b) 6 states, (c) 8 states, and (d) 10 states. Here, $L = 200$, $V = 3$, $\chi = 1000$, and other parameters consistent with the manuscript.

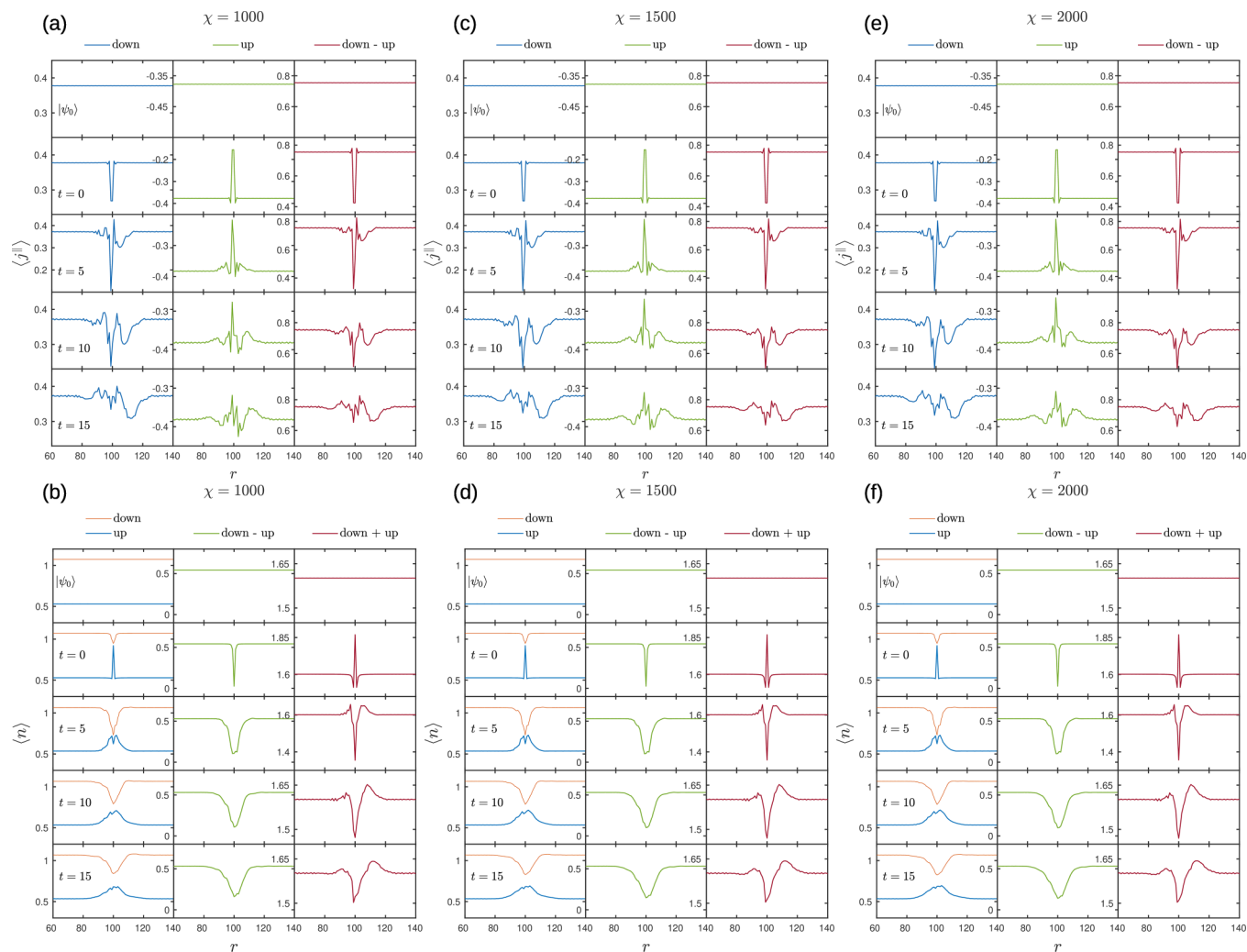


FIG. 9. Snapshots of the time evolution of local particle density $\langle n_{\ell,r}^{\parallel} \rangle$ [(a), (c), (e)] and local leg current configurations $\langle j_{\ell,r}^{\parallel} \rangle$ [(b), (d), (f)] with varying maximum bond dimensions. (a) and (b) correspond to $\chi = 1000$, (c) and (d) correspond to $\chi = 1500$, and (e) and (f) correspond to $\chi = 2000$. Here, $L = 200$, $V = 3$, and other parameters are consistent with the manuscript.

$cutoff = 10^{-6}$ requires χ up to 12 000. The results are shown in Fig. 11. Similar to the other tests, there are also deviations in the currents, and yet the local particle densities exhibit better convergence. For the outwards propagating vortices on both sides, the shape of wavepackets are vague in the currents, while it is easier to identify them in the local particle densities. The asymmetry between the vortices on the two sides has emerged in Fig. 11, which remains consistent across all the tests. Due to the tremendous time consumption, the simulation with only fixed discarded weight in Fig. 11 cannot be extended to longer times. For subsequent propagation, where vortices either propagate ballistically or dissolve, increased errors in the simulations becomes inevitable.

Based on these tests above, we conclude that the asymmetry exists while the data for local observables has numerical errors for the chosen control parameters in the main text. On the one hand, the appearance of asymmetry in Fig. 11 can exclude the possibility of this asymmetry stemming from the additional errors caused by simulating with fixed bond dimension. On the other hand, the comparison involving varying χ , L , and maximum numbers of local boson states in Figs. 7–11 demonstrate their independence from the emergence of asymmetry. But the increased errors in the simulation of subsequent propagation should be noted. In subsequent quantitative studies, improved computational accuracy is necessary.

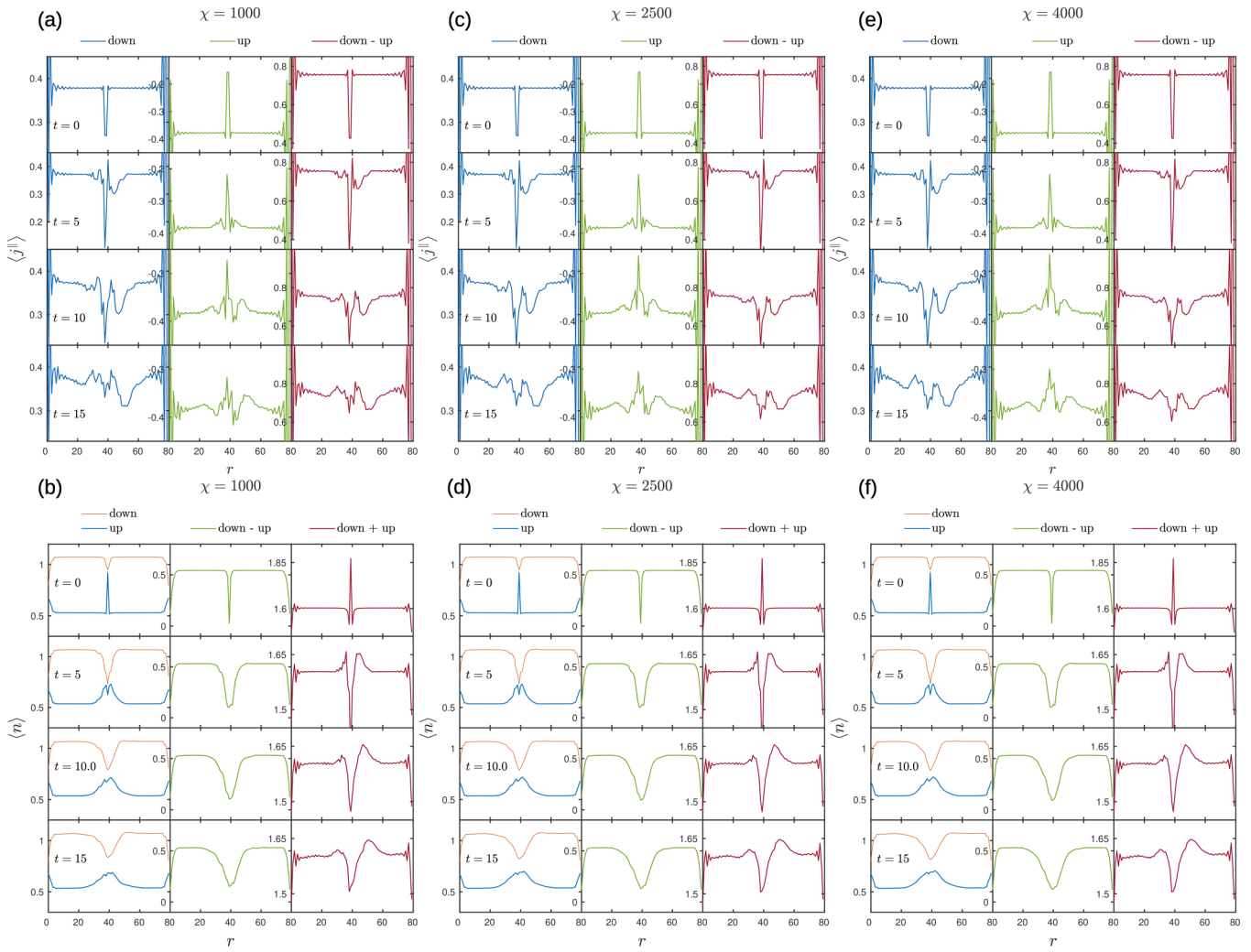


FIG. 10. Snapshots of the time evolution of local particle density $\langle n_{\ell,r}^{\parallel} \rangle$ [(a), (c), (e)] and local leg current configurations $\langle j_{\ell,r}^{\parallel} \rangle$ [(b), (d), (f)] with varying maximum bond dimensions. (a) and (b) correspond to $\chi = 1000$, (c) and (d) correspond to $\chi = 2500$, and (e) and (f) correspond to $\chi = 4000$. Here, $L = 80$, $V = 3$, and other parameters are consistent with the manuscript.

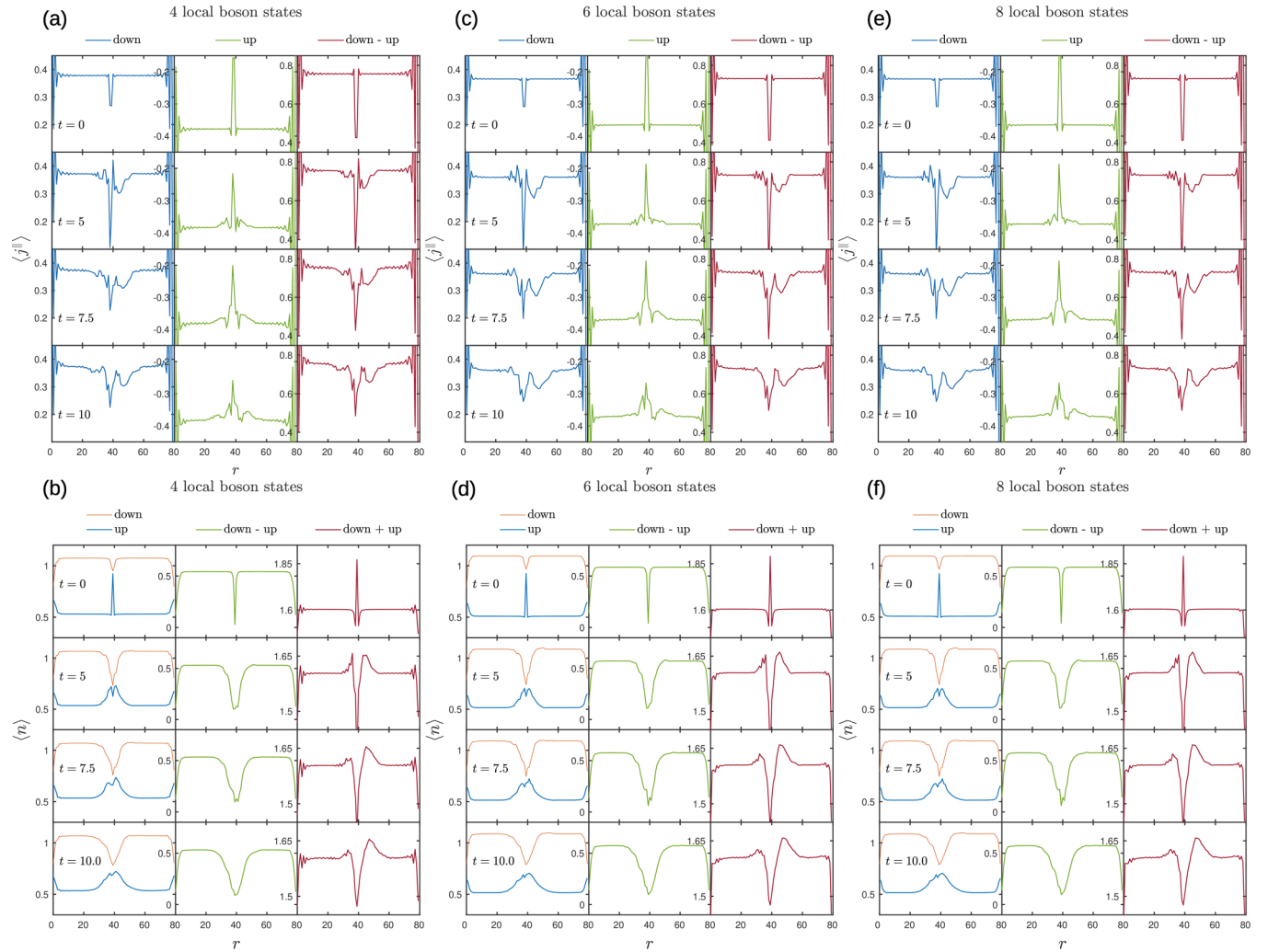


FIG. 11. Snapshots of the time evolution of local particle density $\langle n_{\ell,r}^{\parallel} \rangle$ [(a), (c), (e)] and local leg current configurations $\langle j_{\ell,r}^{\parallel} \rangle$ [(b), (d), (f)] with varying maximum bond dimensions. (a) and (b) correspond to 4 states, (c) and (d) correspond to 6 states, and (e) and (f) correspond to 8 states. Here, we simulate to $t = 10$ with only fixed discarded weight $cutoff = 10^{-6}$ and do not restrict maximum bond dimension. $L = 80$, $V = 3$, and other parameters are consistent with the manuscript.

- [1] I. Ichinose and T. Matsui, Lattice gauge theory for condensed matter physics: Ferromagnetic superconductivity as its example, *Mod. Phys. Lett. B* **28**, 1430012 (2014).
- [2] U.-J. Wiese, Towards quantum simulating QCD, *Nucl. Phys. A* **931**, 246 (2014).
- [3] E. Zohar, J. I. Cirac, and B. Reznik, Quantum simulations of lattice gauge theories using ultracold atoms in optical lattices, *Rep. Prog. Phys.* **79**, 014401 (2016).
- [4] N. Brunner, D. Cavalcanti, S. Pironio, V. Scarani, and S. Wehner, Bell nonlocality, *Rev. Mod. Phys.* **86**, 419 (2014).
- [5] C. L. Degen, F. Reinhard, and P. Cappellaro, Quantum sensing, *Rev. Mod. Phys.* **89**, 035002 (2017).
- [6] I. M. Georgescu, S. Ashhab, and F. Nori, Quantum simulation, *Rev. Mod. Phys.* **86**, 153 (2014).
- [7] J. Preskill, Quantum computing in the NISQ era and beyond, *Quantum* **2**, 79 (2018).
- [8] D. Banerjee, M. Bögli, M. Dalmonte, E. Rico, P. Stebler, U.-J. Wiese, and P. Zoller, Atomic quantum simulation of $U(N)$ and $SU(N)$ non-Abelian lattice gauge theories, *Phys. Rev. Lett.* **110**, 125303 (2013).
- [9] S. Barrett, K. Hammerer, S. Harrison, T. E. Northup, and T. J. Osborne, Simulating quantum fields with cavity QED, *Phys. Rev. Lett.* **110**, 090501 (2013).
- [10] A. W. Glaetzle, M. Dalmonte, R. Nath, I. Rouschatzakis, R. Moessner, and P. Zoller, Quantum spin-ice and dimer models with Rydberg atoms, *Phys. Rev. X* **4**, 041037 (2014).
- [11] A. W. Glaetzle, M. Dalmonte, R. Nath, C. Gross, I. Bloch, and P. Zoller, Designing frustrated quantum magnets with laser-dressed Rydberg atoms, *Phys. Rev. Lett.* **114**, 173002 (2015).
- [12] P. Hauke, D. Marcos, M. Dalmonte, and P. Zoller, Quantum simulation of a lattice Schwinger model in a chain of trapped ions, *Phys. Rev. X* **3**, 041018 (2013).

- [13] L. Homeier, A. Bohrdt, S. Linsel, E. Demler, J. C. Halimeh, and F. Grusdt, Realistic scheme for quantum simulation of \mathbb{Z}_2 lattice gauge theories with dynamical matter in $(2 + 1)d$, *Commun. Phys.* **6**, 127 (2023).
- [14] A. Mezzacapo, E. Rico, C. Sabín, I. L. Egusquiza, L. Lamata, and E. Solano, Non-Abelian SU(2) lattice gauge theories in superconducting circuits, *Phys. Rev. Lett.* **115**, 240502 (2015).
- [15] L. Tagliacozzo, A. Celi, P. Orland, M. W. Mitchell, and M. Lewenstein, Simulation of non-Abelian gauge theories with optical lattices, *Nat. Commun.* **4**, 2615 (2013).
- [16] D. Banerjee, M. Dalmonte, M. Müller, E. Rico, P. Stebler, U.-J. Wiese, and P. Zoller, Atomic quantum simulation of dynamical gauge fields coupled to fermionic matter: From string breaking to evolution after a quench, *Phys. Rev. Lett.* **109**, 175302 (2012).
- [17] H. P. Büchler, M. Hermele, S. D. Huber, M. P. A. Fisher, and P. Zoller, Atomic quantum simulator for lattice gauge theories and ring exchange models, *Phys. Rev. Lett.* **95**, 040402 (2005).
- [18] T. Byrnes and Y. Yamamoto, Simulating lattice gauge theories on a quantum computer, *Phys. Rev. A* **73**, 022328 (2006).
- [19] L. Tagliacozzo, A. Celi, A. Zamora, and M. Lewenstein, Optical Abelian lattice gauge theories, *Ann. Phys.* **330**, 160 (2013).
- [20] E. Zohar and B. Reznik, Confinement and lattice quantum-electrodynamic electric flux tubes simulated with ultracold atoms, *Phys. Rev. Lett.* **107**, 275301 (2011).
- [21] X. Guan, Y. Feng, Z.-Y. Xue, G. Chen, and S. Jia, Synthetic gauge field and chiral physics on two-leg superconducting circuits, *Phys. Rev. A* **102**, 032610 (2020).
- [22] C. Kokail, C. Maier, R. Van Bijnen, T. Brydges, M. K. Joshi, P. Jurcevic, C. A. Muschik, P. Silvi, R. Blatt, C. F. Roos, and P. Zoller, Self-verifying variational quantum simulation of lattice models, *Nature (London)* **569**, 355 (2019).
- [23] E. A. Martinez, C. A. Muschik, P. Schindler, D. Nigg, A. Erhard, M. Heyl, P. Hauke, M. Dalmonte, T. Monz, P. Zoller, and R. Blatt, Real-time dynamics of lattice gauge theories with a few-qubit quantum computer, *Nature (London)* **534**, 516 (2016).
- [24] A. Mil, T. V. Zache, A. Hegde, A. Xia, R. P. Bhatt, M. K. Oberthaler, P. Hauke, J. Berges, and F. Jendrzejewski, A scalable realization of local U(1) gauge invariance in cold atomic mixtures, *Science* **367**, 1128 (2020).
- [25] C. Schweizer, F. Grusdt, M. Berngruber, L. Barbiero, E. Demler, N. Goldman, I. Bloch, and M. Aidelsburger, Floquet approach to \mathbb{Z}_2 lattice gauge theories with ultracold atoms in optical lattices, *Nat. Phys.* **15**, 1168 (2019).
- [26] B. Yang, H. Sun, R. Ott, H.-Y. Wang, T. V. Zache, J. C. Halimeh, Z.-S. Yuan, P. Hauke, and J.-W. Pan, Observation of gauge invariance in a 71-site Bose-Hubbard quantum simulator, *Nature (London)* **587**, 392 (2020).
- [27] F. M. Surace, P. P. Mazza, G. Giudici, A. Lerose, A. Gambassi, and M. Dalmonte, Lattice gauge theories and string dynamics in Rydberg atom quantum simulators, *Phys. Rev. X* **10**, 021041 (2020).
- [28] M. E. Tai, A. Lukin, M. Rispoli, R. Schittko, T. Menke, D. Borgnia, P. M. Preiss, F. Grusdt, A. M. Kaufman, and M. Greiner, Microscopy of the interacting Harper-Hofstadter model in the few-body limit, *Nature (London)* **546**, 519 (2017).
- [29] M. C. Bañuls, R. Blatt, J. Catani, A. Celi, J. I. Cirac, M. Dalmonte, L. Fallani, K. Jansen, M. Lewenstein, S. Montangero, C. A. Muschik, B. Reznik, E. Rico, L. Tagliacozzo, K. Van Acoleyen, F. Verstraete, U.-J. Wiese, M. Wingate, J. Zakrzewski, and P. Zoller, Simulating lattice gauge theories within quantum technologies, *Eur. Phys. J. D* **74**, 165 (2020).
- [30] M. Dalmonte and S. Montangero, Lattice gauge theory simulations in the quantum information era, *Contemp. Phys.* **57**, 388 (2016).
- [31] E. Zohar, Quantum simulation of lattice gauge theories in more than one space dimension—requirements, challenges and methods, *Philos. Trans. R. Soc. London A* **380**, 20210069 (2022).
- [32] T. Ozawa and H. M. Price, Topological quantum matter in synthetic dimensions, *Nat. Rev. Phys.* **1**, 349 (2019).
- [33] M. Aidelsburger, M. Atala, M. Lohse, J. T. Barreiro, B. Paredes, and I. Bloch, Realization of the Hofstadter Hamiltonian with ultracold atoms in optical lattices, *Phys. Rev. Lett.* **111**, 185301 (2013).
- [34] E. Alba, X. Fernandez-Gonzalvo, J. Mur-Petit, J. K. Pachos, and J. J. Garcia-Ripoll, Seeing topological order in time-of-flight measurements, *Phys. Rev. Lett.* **107**, 235301 (2011).
- [35] O. Boada, A. Celi, J. I. Latorre, and V. Picó, Simulation of gauge transformations on systems of ultracold atoms, *New J. Phys.* **12**, 113055 (2010).
- [36] N. Goldman, A. Kubasiak, P. Gaspard, and M. Lewenstein, Ultracold atomic gases in non-Abelian gauge potentials: The case of constant wilson loop, *Phys. Rev. A* **79**, 023624 (2009).
- [37] D. Jaksch and P. Zoller, Creation of effective magnetic fields in optical lattices: The Hofstadter butterfly for cold neutral atoms, *New J. Phys.* **5**, 56 (2003).
- [38] D. Jaksch and P. Zoller, The cold atom Hubbard toolbox, *Ann. Phys.* **315**, 52 (2005).
- [39] G. Juzeliūnas, J. Ruseckas, A. Jacob, L. Santos, and P. Öhberg, Double and negative reflection of cold atoms in non-Abelian gauge potentials, *Phys. Rev. Lett.* **100**, 200405 (2008).
- [40] H. Miyake, G. A. Siviloglou, C. J. Kennedy, W. C. Burton, and W. Ketterle, Realizing the Harper Hamiltonian with laser-assisted tunneling in optical lattices, *Phys. Rev. Lett.* **111**, 185302 (2013).
- [41] E. J. Mueller, Artificial electromagnetism for neutral atoms: Escher staircase and Laughlin liquids, *Phys. Rev. A* **70**, 041603(R) (2004).
- [42] K. Osterloh, M. Baig, L. Santos, P. Zoller, and M. Lewenstein, Cold atoms in non-Abelian gauge potentials: From the Hofstadter “moth” to lattice gauge theory, *Phys. Rev. Lett.* **95**, 010403 (2005).
- [43] B. Paredes and I. Bloch, Minimum instances of topological matter in an optical plaquette, *Phys. Rev. A* **77**, 023603 (2008).
- [44] J. Ruseckas, G. Juzeliūnas, P. Öhberg, and M. Fleischhauer, Non-Abelian gauge potentials for ultracold atoms with degenerate dark states, *Phys. Rev. Lett.* **95**, 010404 (2005).
- [45] A. S. Sørensen, E. Demler, and M. D. Lukin, Fractional quantum Hall states of atoms in optical lattices, *Phys. Rev. Lett.* **94**, 086803 (2005).
- [46] O. Boada, A. Celi, J. I. Latorre, and M. Lewenstein, Quantum simulation of an extra dimension, *Phys. Rev. Lett.* **108**, 133001 (2012).
- [47] A. Celi, P. Massignan, J. Ruseckas, N. Goldman, I. B. Spielman, G. Juzeliūnas, and M. Lewenstein, Synthetic gauge fields in synthetic dimensions, *Phys. Rev. Lett.* **112**, 043001 (2014).
- [48] D. Hügél and B. Paredes, Chiral ladders and the edges of Chern insulators, *Phys. Rev. A* **89**, 023619 (2014).

- [49] M. Calvanese Strinati, E. Cornfeld, D. Rossini, S. Barbarino, M. Dalmonte, R. Fazio, E. Sela, and L. Mazza, Laughlin-like states in bosonic and fermionic atomic synthetic ladders, *Phys. Rev. X* **7**, 021033 (2017).
- [50] A. Petrescu and K. Le Hur, Chiral Mott insulators, meissner effect, and Laughlin states in quantum ladders, *Phys. Rev. B* **91**, 054520 (2015).
- [51] L. Taddia, E. Cornfeld, D. Rossini, L. Mazza, E. Sela, and R. Fazio, Topological fractional pumping with alkaline-earth-like atoms in synthetic lattices, *Phys. Rev. Lett.* **118**, 230402 (2017).
- [52] S. Greschner, M. Filippone, and T. Giamarchi, Universal Hall response in interacting quantum systems, *Phys. Rev. Lett.* **122**, 083402 (2019).
- [53] D. Genkina, L. M. Aycok, H.-I. Lu, M. Lu, A. M. Pineiro, and I. B. Spielman, Imaging topology of Hofstadter Ribbons, *New J. Phys.* **21**, 053021 (2019).
- [54] M. Mancini, G. Pagano, G. Cappellini, L. Livi, M. Rider, J. Catani, C. Sias, P. Zoller, M. Inguscio, M. Dalmonte, and L. Fallani, Observation of chiral edge states with neutral fermions in synthetic Hall Ribbons, *Science* **349**, 1510 (2015).
- [55] B. K. Stuhl, H.-I. Lu, L. M. Aycok, D. Genkina, and I. B. Spielman, Visualizing edge states with an atomic Bose gas in the quantum Hall regime, *Science* **349**, 1514 (2015).
- [56] M. Buser, C. Hubig, U. Schollwöck, L. Tarruell, and F. Heidrich-Meisner, Interacting bosonic flux ladders with a synthetic dimension: Ground-state phases and quantum quench dynamics, *Phys. Rev. A* **102**, 053314 (2020).
- [57] M. Mamaev, T. Bilitewski, B. Sundar, and A. M. Rey, Resonant dynamics of strongly interacting $SU(n)$ fermionic atoms in a synthetic flux ladder, *PRX Quantum* **3**, 030328 (2022).
- [58] M. Buser, S. Greschner, U. Schollwöck, and T. Giamarchi, Probing the Hall voltage in synthetic quantum systems, *Phys. Rev. Lett.* **126**, 030501 (2021).
- [59] M. Buser, U. Schollwöck, and F. Grusdt, Snapshot-based characterization of particle currents and the hall response in synthetic flux lattices, *Phys. Rev. A* **105**, 033303 (2022).
- [60] T.-W. Zhou, G. Cappellini, D. Tusi, L. Franchi, J. Parravicini, C. Repellin, S. Greschner, M. Inguscio, T. Giamarchi, M. Filippone, J. Catani, and L. Fallani, Observation of universal Hall response in strongly interacting fermions, *Science* **381**, 427 (2023).
- [61] E. Orignac and T. Giamarchi, Meissner effect in a bosonic ladder, *Phys. Rev. B* **64**, 144515 (2001).
- [62] M. Calvanese Strinati, R. Berkovits, and E. Shimshoni, Emergent bosons in the fermionic two-leg flux ladder, *Phys. Rev. B* **100**, 245149 (2019).
- [63] M. Calvanese Strinati, S. Sahoo, K. Shtengel, and E. Sela, Pretopological fractional excitations in the two-leg flux ladder, *Phys. Rev. B* **99**, 245101 (2019).
- [64] A. Dhar, T. Mishra, M. Maji, R. V. Pai, S. Mukerjee, and A. Paramekanti, Chiral Mott insulator with staggered loop currents in the fully frustrated Bose-Hubbard model, *Phys. Rev. B* **87**, 174501 (2013).
- [65] M. Di Dio, S. De Palo, E. Orignac, R. Citro, and M.-L. Chiofalo, Persisting meissner state and incommensurate phases of hardcore boson ladders in a flux, *Phys. Rev. B* **92**, 060506(R) (2015).
- [66] S. Greschner, M. Piraud, F. Heidrich-Meisner, I. P. McCulloch, U. Schollwöck, and T. Vekua, Spontaneous increase of magnetic flux and chiral-current reversal in bosonic ladders: Swimming against the tide, *Phys. Rev. Lett.* **115**, 190402 (2015).
- [67] S. Greschner, M. Piraud, F. Heidrich-Meisner, I. P. McCulloch, U. Schollwöck, and T. Vekua, Symmetry-broken states in a system of interacting bosons on a two-leg ladder with a uniform Abelian gauge field, *Phys. Rev. A* **94**, 063628 (2016).
- [68] S. Greschner and T. Vekua, Vortex-hole duality: A unified picture of weak- and strong-coupling regimes of bosonic ladders with flux, *Phys. Rev. Lett.* **119**, 073401 (2017).
- [69] C.-M. Halati and T. Giamarchi, Bose-Hubbard triangular ladder in an artificial gauge field, *Phys. Rev. Res.* **5**, 013126 (2023).
- [70] D. Johnstone, P. Öhberg, and C. W. Duncan, Interacting bosons on crystalline and quasiperiodic ladders in a magnetic field, *Phys. Rev. Res.* **5**, 023195 (2023).
- [71] X.-X. Li, R.-J. Cheng, J.-L. Ma, A.-X. Zhang, and J.-K. Xue, Solitary matter wave in spin-orbit-coupled Bose-Einstein condensates with helicoidal gauge potential, *Phys. Rev. E* **104**, 034214 (2021).
- [72] S. Liang, Z.-W. Wang, J. Qin, X.-D. Zhao, and L. Zhou, Collective dipole oscillations in a bosonic ladder lattice with effective magnetic flux, *Results Phys.* **29**, 104678 (2021).
- [73] A. Petrescu and K. Le Hur, Bosonic Mott insulator with Meissner currents, *Phys. Rev. Lett.* **111**, 150601 (2013).
- [74] M. Piraud, F. Heidrich-Meisner, I. P. McCulloch, S. Greschner, T. Vekua, and U. Schollwöck, Vortex and meissner phases of strongly interacting bosons on a two-leg ladder, *Phys. Rev. B* **91**, 140406(R) (2015).
- [75] X. Qiao, X.-B. Zhang, Y. Jian, A.-X. Zhang, Z.-F. Yu, and J.-K. Xue, Quantum phases of interacting bosons on biased two-leg ladders with magnetic flux, *Phys. Rev. A* **104**, 053323 (2021).
- [76] Y.-F. Song and S.-J. Yang, Quantum phases for bosons in a magnetic lattice with a harmonic trap, *New J. Phys.* **22**, 073001 (2020).
- [77] R. Wei and E. J. Mueller, Theory of bosons in two-leg ladders with large magnetic fields, *Phys. Rev. A* **89**, 063617 (2014).
- [78] U. Schollwöck, The density-matrix renormalization group in the age of matrix product states, *Ann. Phys.* **326**, 96 (2011).
- [79] M. Fishman, S. R. White, and E. M. Stoudenmire, The ITensor software library for tensor network calculations, *SciPost Phys. Codebases* **004** (2022).
- [80] H. Saberi, A. Weichselbaum, and J. von Delft, Matrix-product-state comparison of the numerical renormalization group and the variational formulation of the density-matrix renormalization group, *Phys. Rev. B* **78**, 035124 (2008).
- [81] S. R. White, Density-matrix algorithms for quantum renormalization groups, *Phys. Rev. B* **48**, 10345 (1993).
- [82] A. E. Feiguin, The density matrix renormalization group and its time-dependent variants, *AIP Conf. Proc.* **1419**, 5 (2011).
- [83] G. Vidal, Classical simulation of infinite-size quantum lattice systems in one spatial dimension, *Phys. Rev. Lett.* **98**, 070201 (2007).
- [84] S. R. White and A. E. Feiguin, Real-time evolution using the density matrix renormalization group, *Phys. Rev. Lett.* **93**, 076401 (2004).
- [85] T. Rakovszky, F. Pollmann, and C. W. Von Keyserlingk, Diffusive hydrodynamics of out-of-time-ordered correlators

- tors with charge conservation, [Phys. Rev. X 8, 031058 \(2018\)](#).
- [86] V. Khemani, A. Vishwanath, and D. A. Huse, Operator spreading and the emergence of dissipative hydrodynamics under unitary evolution with conservation laws, [Phys. Rev. X 8, 031057 \(2018\)](#).
- [87] A. Nahum, J. Ruhman, S. Vijay, and J. Haah, Quantum entanglement growth under random unitary dynamics, [Phys. Rev. X 7, 031016 \(2017\)](#).
- [88] A. Nahum, S. Vijay, and J. Haah, Operator spreading in random unitary circuits, [Phys. Rev. X 8, 021014 \(2018\)](#).
- [89] C. W. von Keyserlingk, T. Rakovszky, F. Pollmann, and S. L. Sondhi, Operator hydrodynamics, OTOCs, and entanglement growth in systems without conservation laws, [Phys. Rev. X 8, 021013 \(2018\)](#).
- [90] D. A. Abanin and Z. Papić, Recent progress in many-body localization: Recent progress in many-body localization, [Annalen der Physik 529, 1700169 \(2017\)](#).
- [91] D. A. Abanin, E. Altman, I. Bloch, and M. Serbyn, *Colloquium*: Many-body localization, thermalization, and entanglement, [Rev. Mod. Phys. 91, 021001 \(2019\)](#).
- [92] E. Altman and R. Vosk, Universal dynamics and renormalization in many-body-localized systems, [Annu. Rev. Condens. Matter Phys. 6, 383 \(2015\)](#).
- [93] S. Gopalakrishnan and S. A. Parameswaran, Dynamics and transport at the threshold of many-body localization, [Phys. Rep. 862, 1 \(2020\)](#).
- [94] R. Nandkishore and D. A. Huse, Many-body localization and thermalization in quantum statistical mechanics, [Annu. Rev. Condens. Matter Phys. 6, 15 \(2015\)](#).